Table S1. Cryo-EM and model refinement statistics

	S. solfataricus **AT4P**	***P. calidifontis*** **flagella-like**	***H. volcanii*** **AT4P**	***A. pernix*** **AFF**	**Asymmetric *S. solfataricus* AT4P reconstruction**
Reconstruction Box size	384 x 384	320 x 320	320 x 320	320 x 320	384 x 384
PDB	8FJS	8FK7	8FJ5	7TXI	8FK0
EMDB	29246	29249	29215	26158	29247
Pixel size (Å)	1.08	1.08	1.08	1.08	1.08
Number of particles	2,703,710	108,016	1,660,828	59,338	95,337
B-factor	-171	-92.5	-123.6	-50	-65.6
Resolution 0.143 FSC Map:Map (Å)	2.9	4.1	2.9	3.5	3.6
Resolution 0.5 FSC Model:Map (Å)	3.0	4.3	3.0	3.9	4.0
Helical Rise (Å)	4.98	4.87	5.16	5.52	N/A
Helical twist (°)	104.57	108.92	106.3	108.0	N/A
Ramachandran favored (%)	96.2	99.3	96.6	93.8	97.4
Ramachandran allowed (%)	3.9	0.7	3.4	5.7	2.6
Ramachandran Outliers (%)	0	0	0	0.5	0
Clash score	4.56	10.26	3.40	13.94	9.67
Molprobity score	1.49	1.53	1.33	2.06	1.62
Bond angles rmsd (°)	0.454	0.558	0.992	1.244	0.555
Bond length RMSD (Å)	0.002	0.003	0.005	0.008	0.003

Table S2. Archaeal Type IV pilin and Flagellin models compared in this study

Species	Type	PDB ID	Length of N-term Helix	Length of linker	Length of C-term Domain
S. solfataricus	AT4P	8FJS (this study)	34	3	95
P. arsenaticum	AT4P	6W8U	32	3	105
S. islandicus LAL14	AT4P	6NAV	34	3	94
H. volcanii	AT4P	8FJ5 (This study)	31	7	95
I hospitalis	AT4P	5KYH	28	8	266
Natrinema J7-2	AT4P	8GI2	29	7	110
P. calidifontis	AT4P	8FK7 (This study)	39	3	93
M. villosus	AFF	7OFQ	47	3	160
M. hungtai	AFF	5TFY	48	2	115
M. maripaludis	AFF	5Z1L	47	2	149
S. islandicus REY15A	AFF	8CWM	47	2	238
A. pernix	AFF	7TXI (This study)	45	2	149
P. furiosus	AFF	5O4U	47	1	158

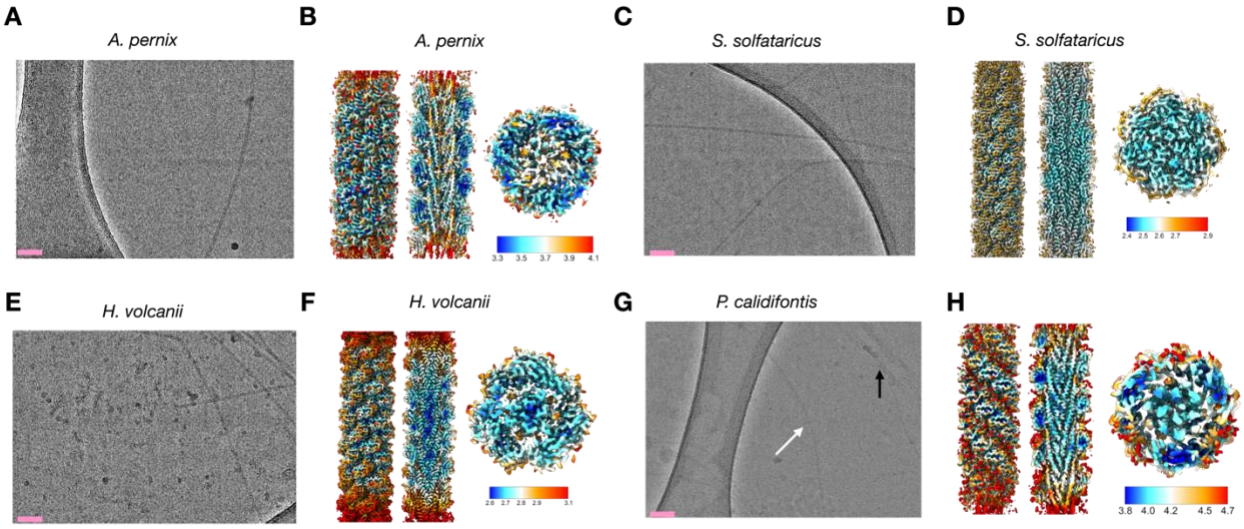

Fig. S1 Cryo-electron micrographs of archaeal filaments. (A,C,E,G) The scale bar in all micrographs is 50 nm. **(A)** Cryo-electron micrograph of the *A. pernix* flagellar filament. **(B**) Local resolution estimate for the *A. pernix* AFF. **(C)** Cryo-electron micrograph of *S. solfataricus* AT4P. **(D)** Local resolution estimate for the *S. solfataricus* AT4P. **(E)** Cryo-electron micrograph of *H. volcanii* AT4P. **(F)** Local resolution estimate for the *H. volcanii* AT4P. **(G)** Cryo-electron micrograph of *P. calidifontis* filaments with the white arrow indicating the flagellar-like AT4P. The black arrow indicates the archaeal bundling pili.

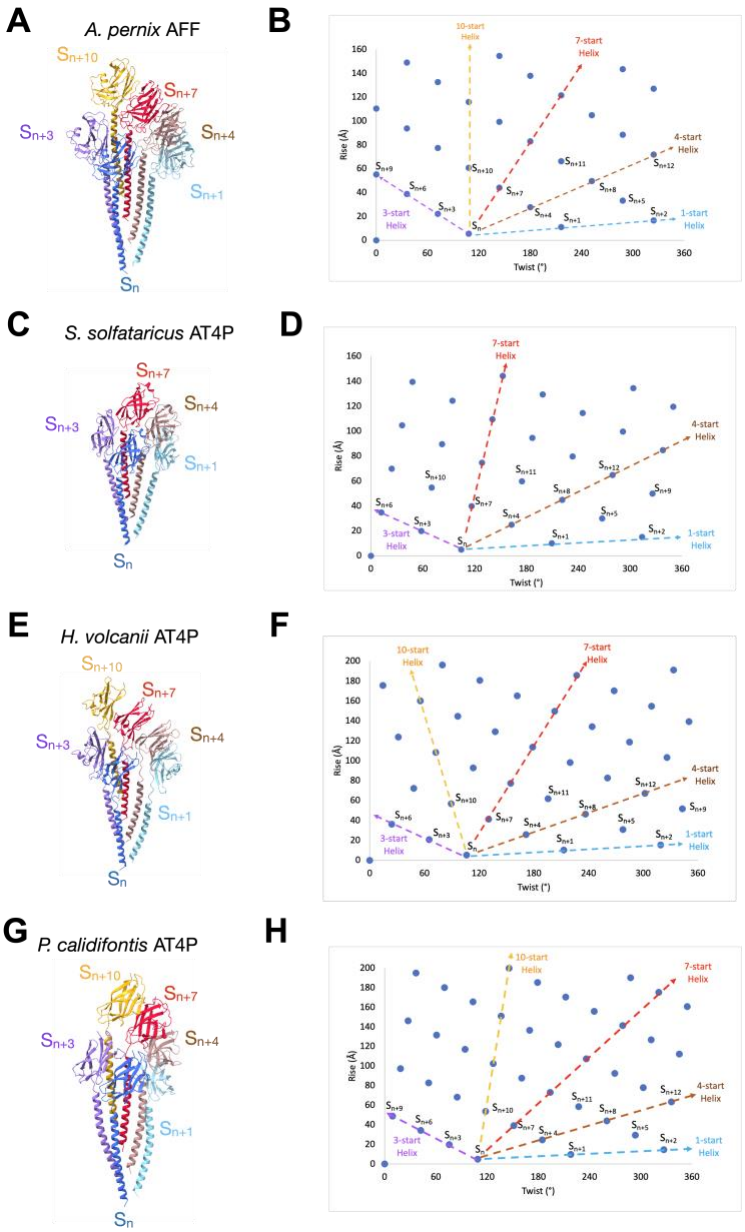

Fig. S2. Subunit contacts in the AT4P and AFF structures from this study. (A) Subunit contacts in the *A. pernix* AFF. A flagellin subunit S_n (dark blue) contacts five other subunits that are 1 (light blue, S_{n+1}), 3 (purple, S_{n+3}), 4 (brown, S_{n+4}), 7 (red, S_{n+7}), and 10 (gold, S_{n+10}) subunits away from its position in the filament along the *A. pernix* 1-start helix. **(B)** Helical net of the *A. pernix* AFF with the 1-start (light blue), 3-start (purple), 4-start (brown), 7-start (red), and 10-start helices (gold) indicated with dashed arrows. **(C)** Subunit contacts in the *S. solfataricus* AT4P. A single *S. solfataricus* pilin makes contacts along its 1-, 3-, 4-, and 7-start interfaces. **(D)** Helical net of the *S. solfataricus* AT4P with the 1-, 3-, 4-, and 7-start helices indicated by dashed arrows. **(E)** Subunit contacts in the *H. volcanii* AT4P. Each *H. volcanii* subunit has contacts along its 1-, 3-, 4-, 7-, and 10-start interfaces. **(F)** Helical net for the *H. volcanii* AT4P with its 1-, 3-, 4-, 7-, and 10-start helices indicated. **(G)** Subunit contacts in the *P. calidifontis* flagellar-like AT4P. Each *P. calidifontis* pilin makes contacts with subunits 1, 3, 4, 7, and 10 subunits away from it in the filament. **(H)** Helical net for the *P. calidifontis* AT4P. The 1-, 3-, 4-, 7-, and 10-start helices are indicated.

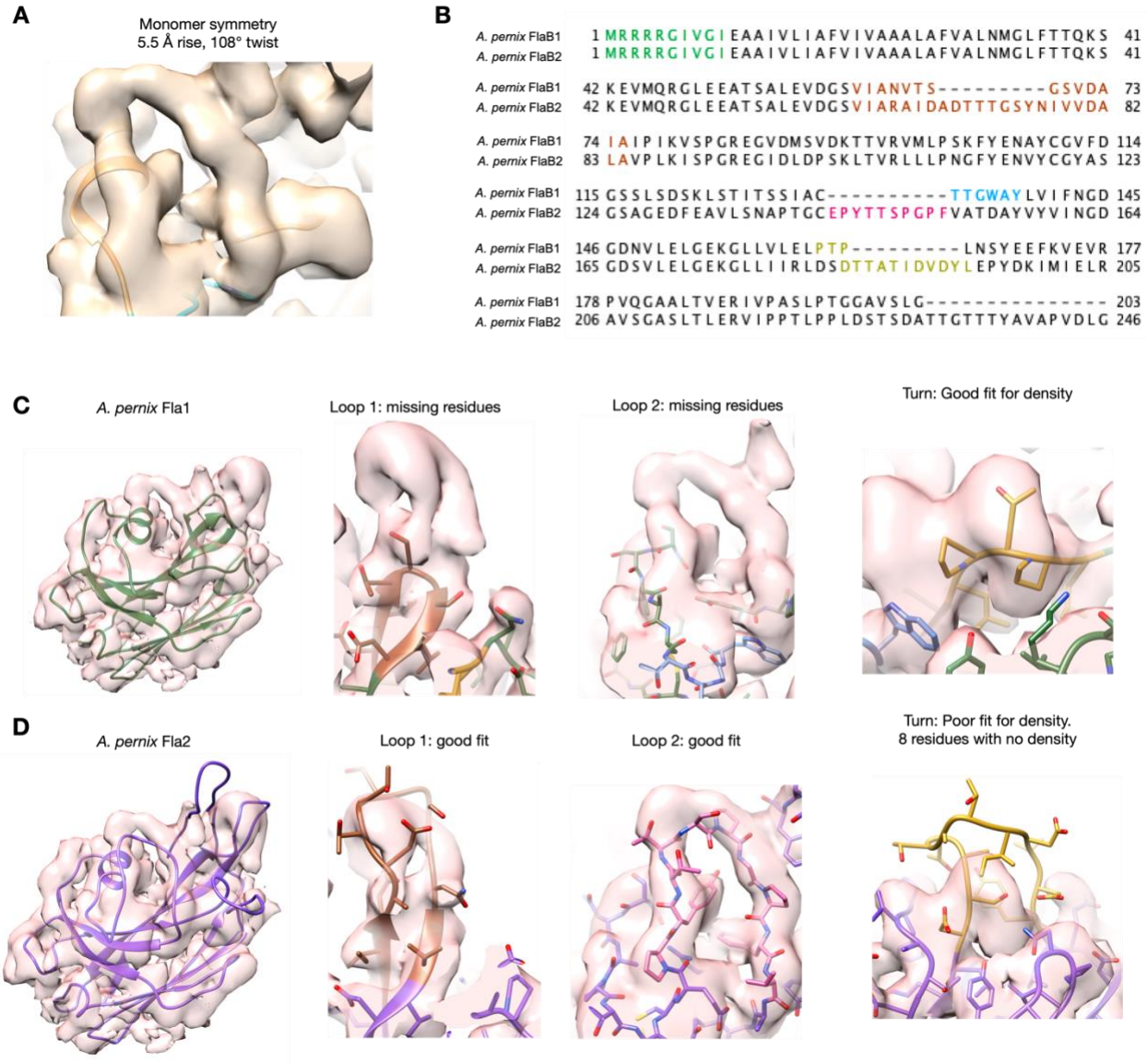

Fig. S3. Structural ambiguities in the *A. pernix* flagellar filament. (A) Density map (EMD 26158) of the *A. pernix* flagellar filament with its model (PDB: 7TXI) fit in. The view of the map is centered around density that appears to be a polypeptide chain with nothing modeled in. **(B)** Sequence alignment of the two *A. pernix* flagellins. The processed signal sequences are shown in green. Regions critical to interpreting the density map are highlighted in different colors. (**C-D)** From left to right the images show the full model and map for a hairpin region (loop 1), the loop indicated in A (loop 2) and an additional region in the density map representing a turn (turn). The color of the protein model in the various regions (brown, blue, pink, and gold) correspond to the colors in **B. (C)** The outer domain model for the *A. pernix* flagellin 1. For loop 1 there are many amino acids not modeled into the density. With loop 2 there are no residues fit into the map. For the turn the model fits the map. **(D)** The outer domain model for *A. pernix* flagellin 2. The sequence fits the loop 1 and loop 2 densities, however there are about 8 residues left unmodeled in the turn, and this does not appear to be due to flexibility.

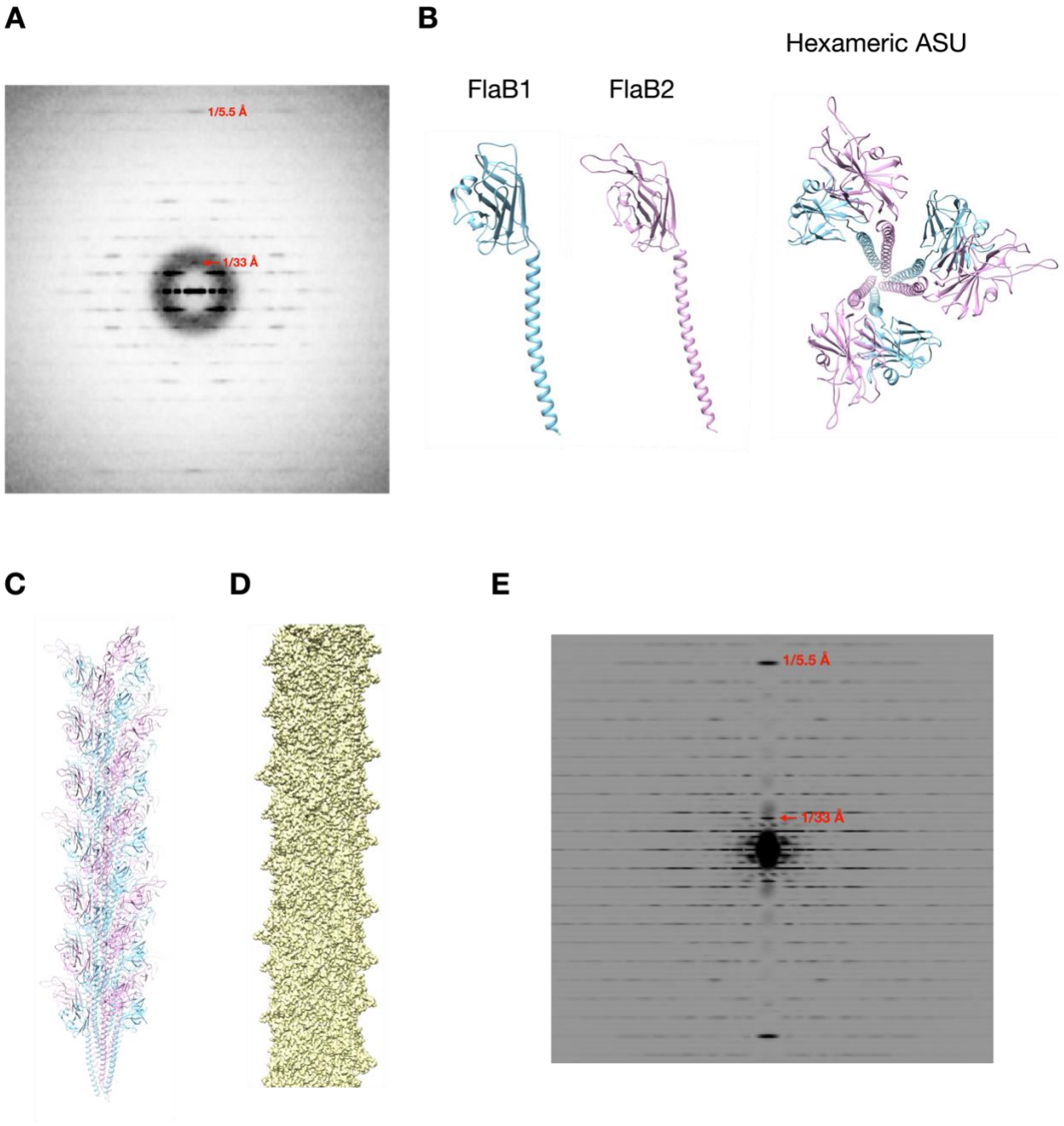

Fig. S4. Possibility of multiple flagellins in the *A. pernix* archaeal flagellar filament. (**A)** Averaged power spectrum of the *A. pernix* flagellar filament image segments. Two meridional layer lines are indicated at 1/(33 Å) and 1/(5.5 Å). The 1/(5.5 Å) meridional arises from the rise per subunit and should be the only meridional intensity seen in this power spectrum if every subunit was equivalent in the filament. However, the 1/(33 Å) meridional arises from an asymmetric unit in the filament containing six subunits (a hexamer). **(B)** Generation of hexameric ASU for the *A. pernix* flagellar filament assuming the same symmetry as reported in Gambelli et al., a helical rise of 33 Å and a twist of -72 °. **(C)** Filament model generated from the hexameric ASU **(D)** Simulated density map generated from the hexameric symmetry *A. pernix* model. **(E)** Power spectrum of 2D projections of the simulated hexameric symmetry density map showing meridional layer lines at 1/(33 Å) and 1/(5.5 Å). The 1/(33 Å) meridional intensity is much stronger in this model power spectrum than in the observed power spectrum (A), suggesting that the observed filaments are a mixture of segments with and without the hexameric ASU.

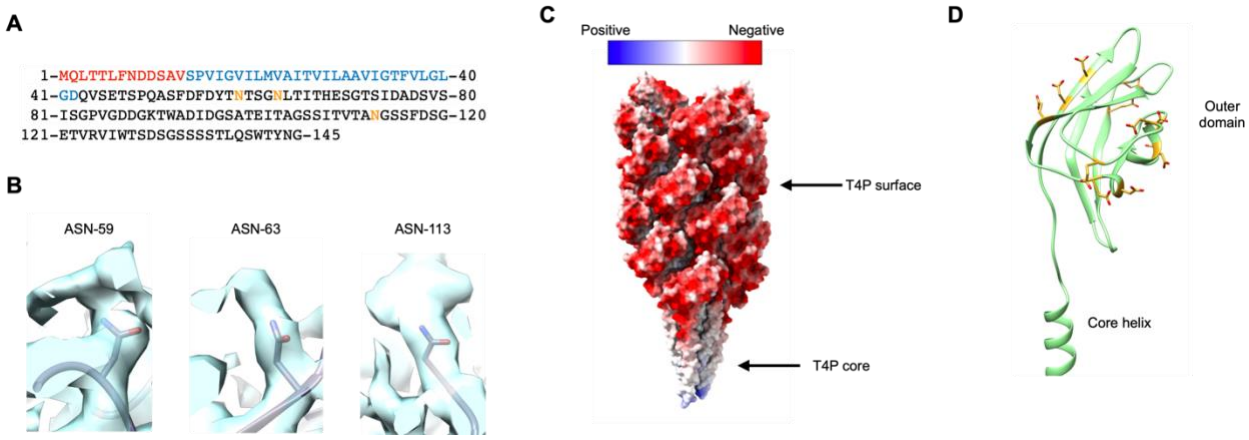

Fig. S5. Glycosylation and negative charge of the *H. volcanii* archaeal T4P. (A) Amino acid sequence of the *H. volcanii* pilin. The N-terminal signal sequence which gets cleaved prior to assembly is in red. The N-terminal core helix residues are in blue. Residues which are glycosylated in the density map are in gold. **(B)** Glycan density for each of the three glycosylated asparagine residues of the *A. pernix* archaeal T4P.**(C)** The electrostatic potential map of the *H. volcanii* T4P. The surface of the T4P is highly negatively charged. **(D)** Depiction of the outer domain of the *H. volcanii* pilin with negatively charged aspartate and glutamate residues colored gold.

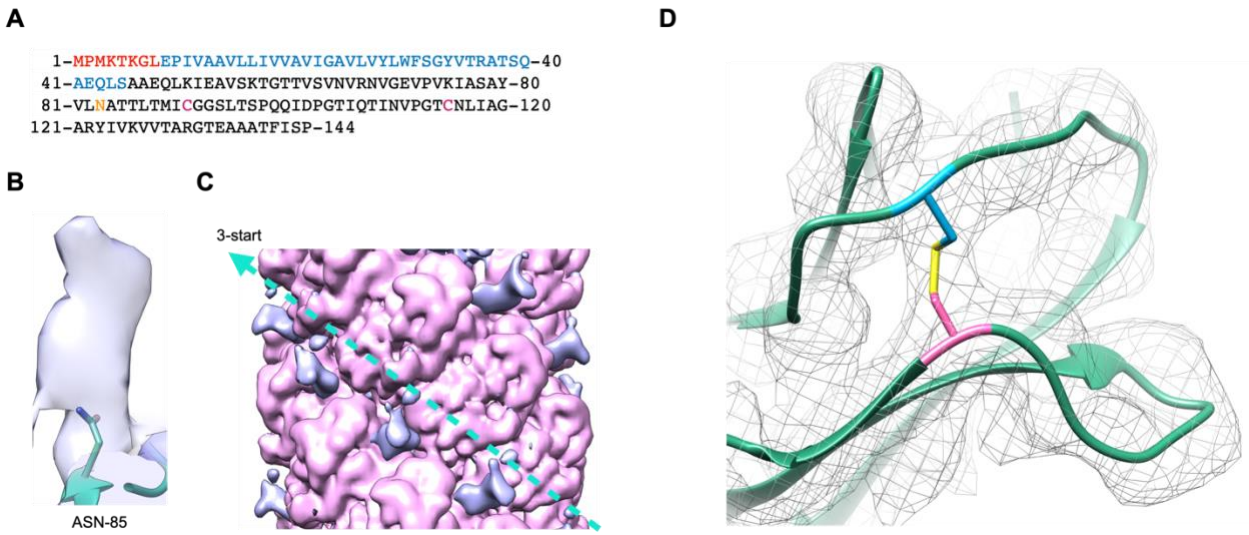

Fig. S6. Glycosylation and disulfide bridges of the *P. calidifontis* flagellar-like T4P. (A) Amino acid sequence of the *P. calidifontis* pilin. The signal sequence is in red, while the N-terminal helix core is in blue. Glycosylated residues are gold and cysteine residues are pink. **(C)** Density map of the *P. calidifontis* T4P with protein density in pink and glycan density in purple. The glycan density forms a series of ridges along the 3-start helix in the grooves between subunits. **(D)** Intramolecular disulfide bridge in the *P. calidifontis* flagellar-like T4P.

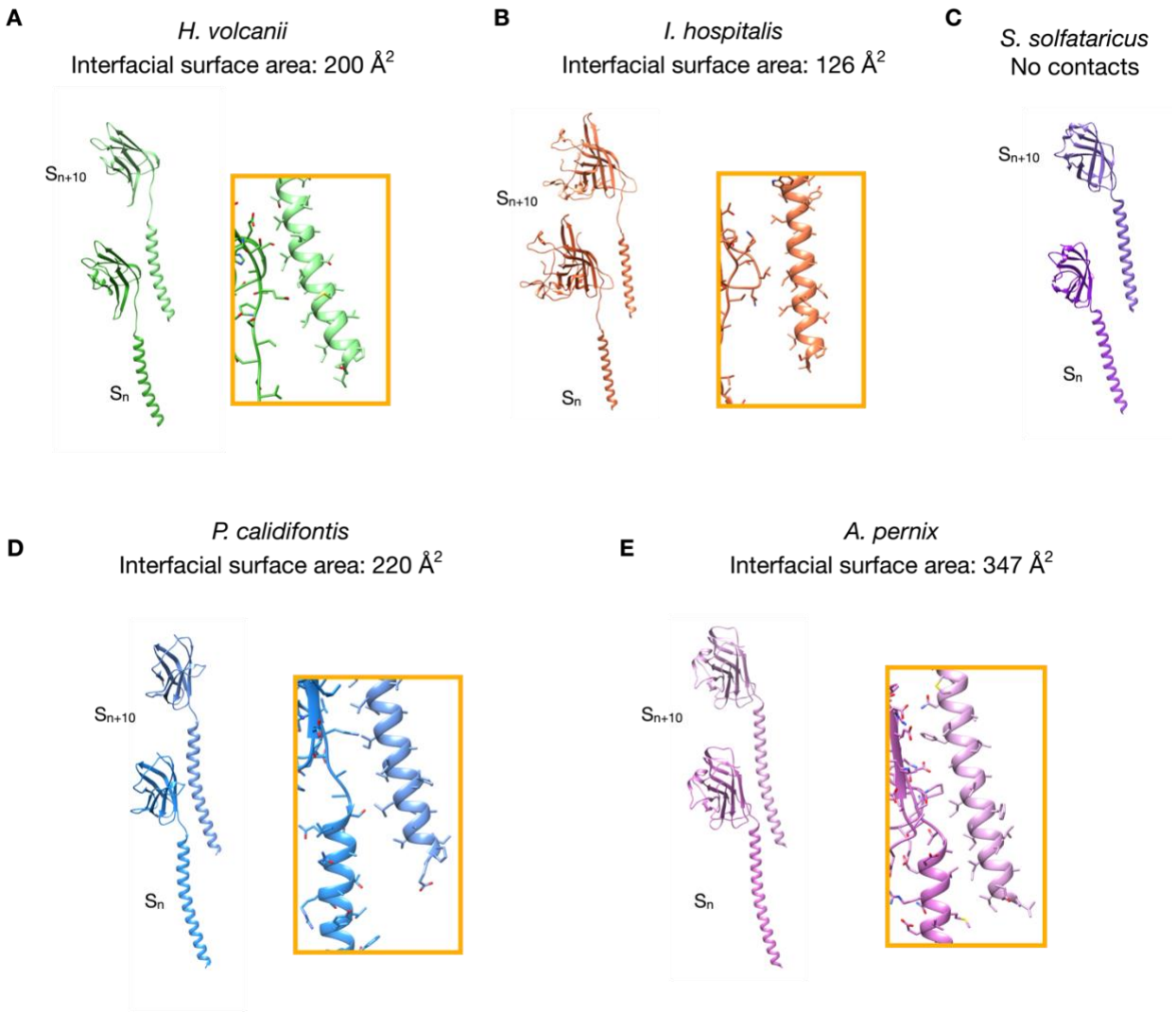

Fig. S7. Full length subunit interactions along the 10-start interface. (A) The 10-start interactions of the *H. volcanii* T4P subunits are shown. A close-up of the 10-start interface is shown in the inset. **(B)** The 10-start interactions for the *I. hospitalis* T4P. **(C)** Two subunits in the 10-start helix are shown for the *S. solfataricus* T4P. No significant contacts are made along this interface. **(D)** The 10-start interfacial contacts between subunits in the *P. calidifontis* flagellar-like filament are shown. **(E)** The 10-start interfacial contacts between subunits in the *A. pernix* archaeal flagellar filament are shown.

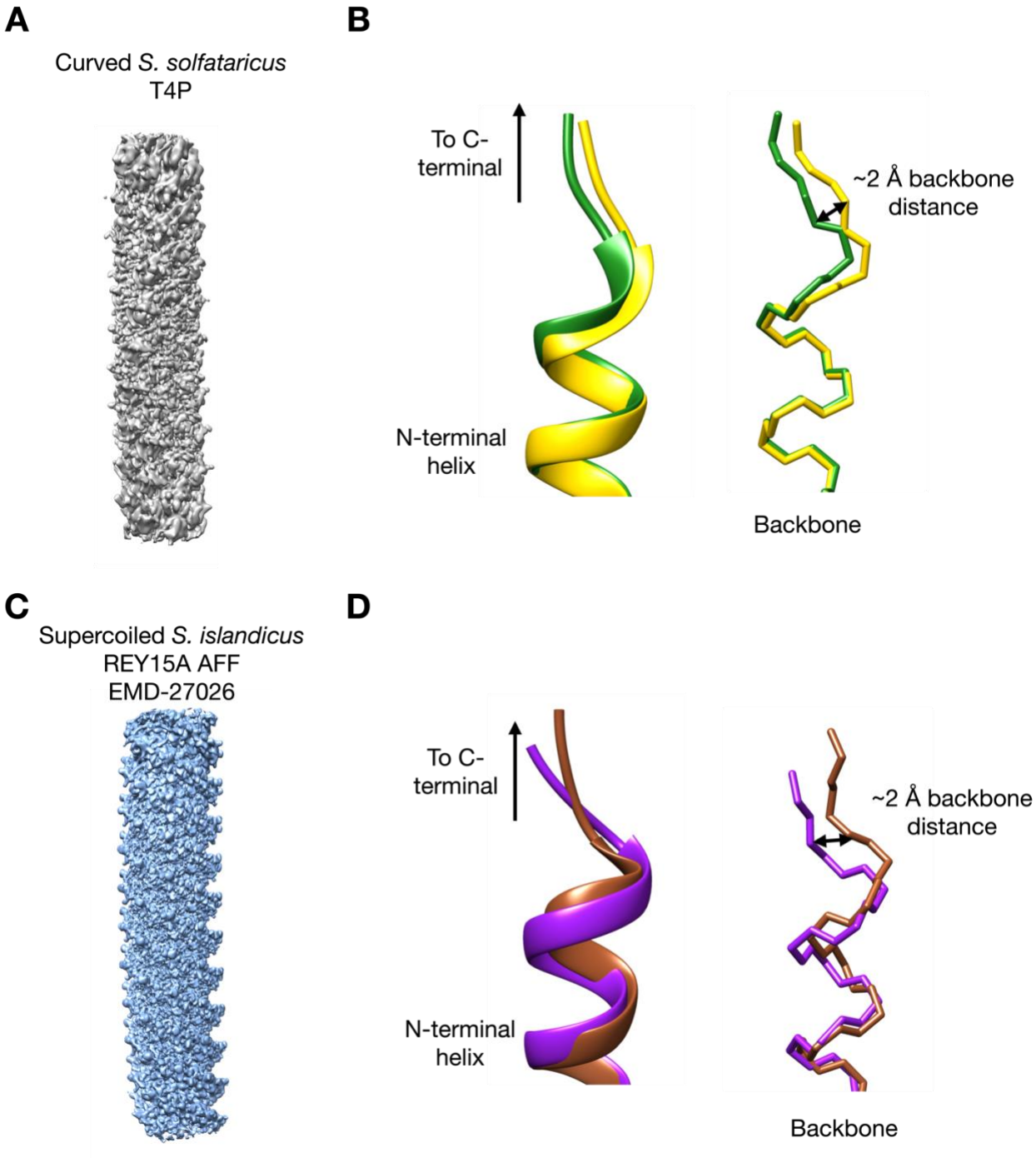

Fig. S8. Comparison of the flexible linker region in curved *S. solfataricus* T4P and supercoiled *S. islandicus* Rey 15A AFF structures. (A) Density map of the curved *S. solfataricus* T4P structure, one of several volumes, generated from 3D variability analysis of curved T4P particles. **(B)** Comparison of the linker regions of subunits from the two most different 7-start strands of the *S. solfataricus* T4P structure. These models were generated using a total of 14 subunits, with two subunits from each of the 7 strands. The subunits were then aligned by their N-terminal helices. **(C)** Density map of the supercoiled *S. islandicus* REY15A archaeal flagellar filament (EMD-27026). **(D)** Comparison of subunits from the two most different REY15A protofilaments from the deposited model (PDB 8CWM).

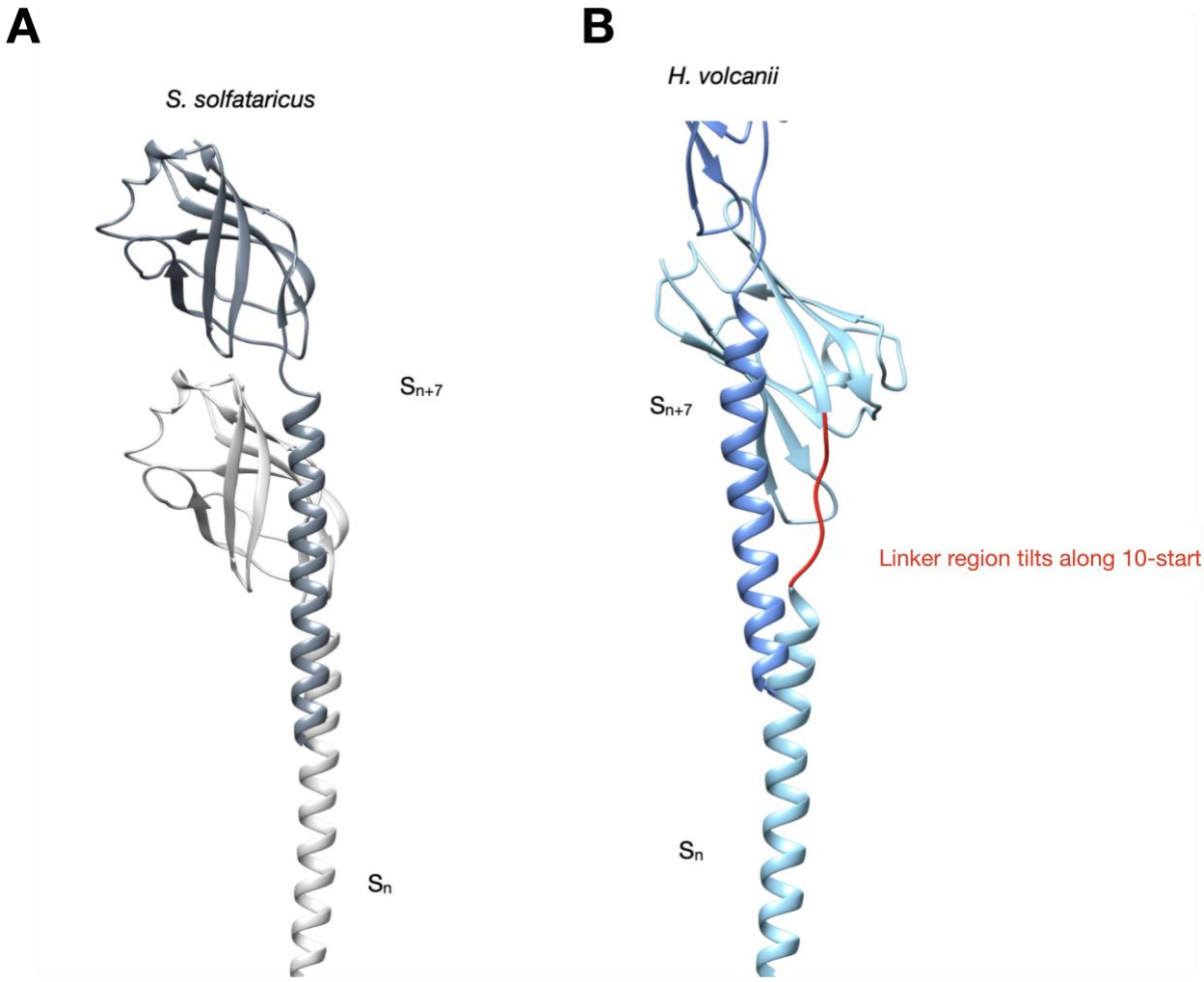

Fig. S9 Comparison of *S. solfataricus* and *H. volcanii* 7-start contacts. (A-B) For both structures the models are viewed from the inside of the filament. As such both filaments' Sn_{+7} subunits are tilted counter-clockwise while elsewhere in the paper the subunits would be displayed with a clockwise tilt. **(A)** Two adjacent *S. solfataricus* type IV pilins (light grey and slate grey) are shown along the 7-start helix. **(B)** Two adjacent *H. volcanii* type IV pilins are shown along the 7-start helix. The extended linker of the *H. volcanii* subunit (red loop in subunit S_n) makes contacts along the 10-start and thus tilts away from the 7-start interface.

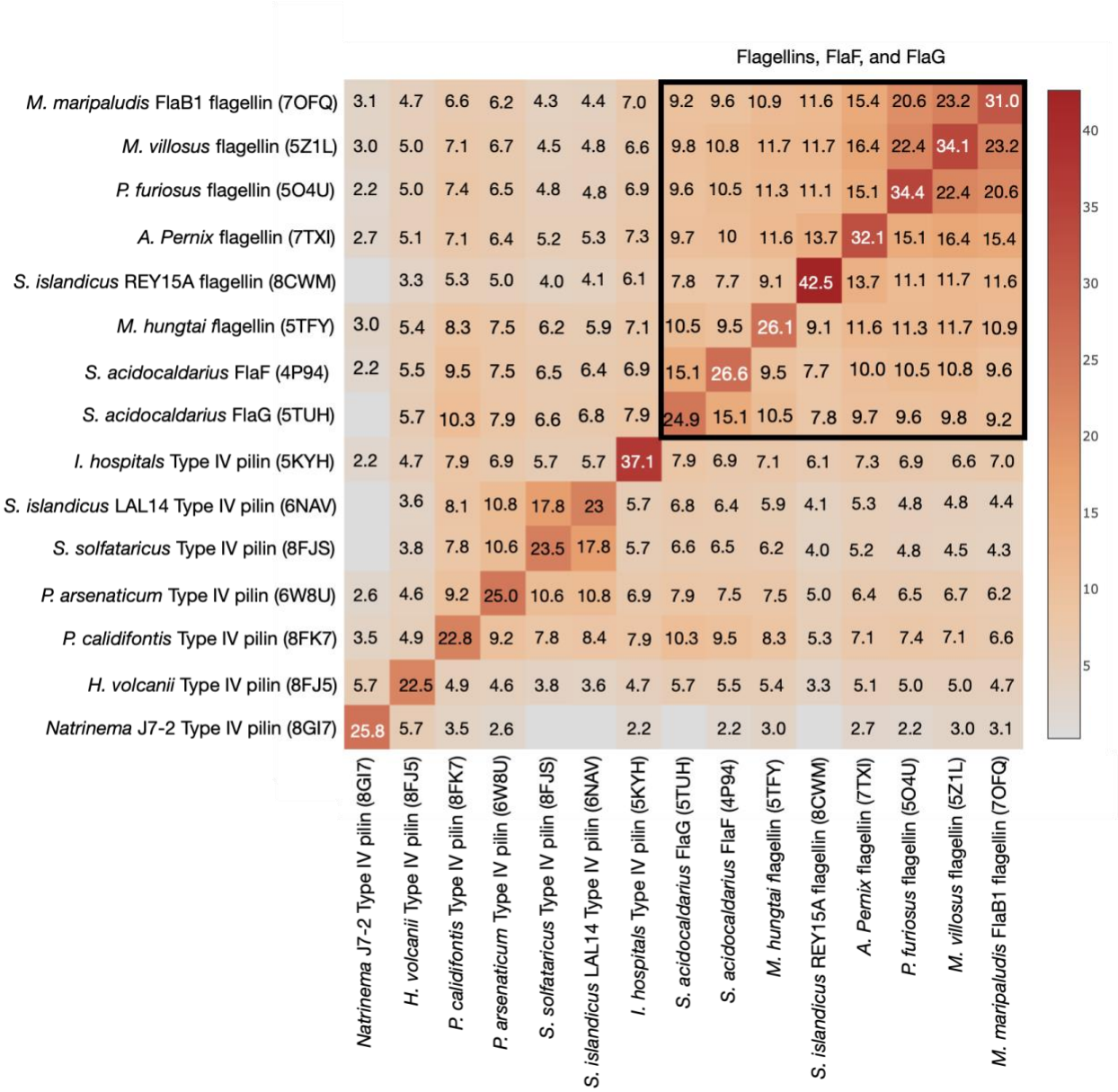

Fig. S10 All-against-all Dali server alignment of **AT4P and AFF C-terminal domains as well as and FlaG and FlaF stator proteins.** The analysis is a comparison of the C-terminal domains of all the structures indicated. PDB IDs are shown for each structure. The Z-score is shown for each pairing. The flagellins versus flagellins, as well as FlaG and FlaF with each other, are enclosed within the black box.